Phys. Status Solidi A **213,** No. 2, 405–411 (2016) / **DOI** 10.1002/pssa.201532033

physica status solidi a
www.pss-a.com
applications and materials science

Camera-based high frequency heterodyne lock-in carrierographic (frequency-domain photoluminescence) imaging of crystalline silicon wafers

Qiming Sun[1,2], Alexander Melnikov[2], and Andreas Mandelis*[,1,2]

[1] School of Optoelectronic Information, University of Electronic Science and Technology of China, Chengdu 610054, P.R. China
[2] Center for Advanced Diffusion-Wave Technologies (CADIFT), Mechanical and Industrial Engineering, University of Toronto, Toronto M5S 3G8, Canada

Received 16 January 2015, revised 21 October 2015, accepted 23 October 2015
Published online 12 November 2015

Keywords cameras, carrierography, heterodyne, imaging, photoluminescence, silicon wafers

* Corresponding author: e-mail mandelis@mie.utoronto.ca, Phone: +1 4169785106, Fax: +1 4162667867

A heterodyne lock-in imaging scheme is introduced to overcome NIR camera speed limitations and poor signal-to-noise ratios, thereby generating high-frequency carrierographic imaging up to 10 kHz. A theoretical model was established to investigate the heterodyne signal generation mechanism as well as to extract the major carrier transport parameters by best-fitting the entire modulation frequency dependence. Good agreement was found between the theoretically predicted and experimentally measured heterodyne amplitude dependence on excitation intensity. A contrast inversion feature in the high-frequency heterodyne amplitude images was observed. High-frequency information presents a method for resolving local near-surface carrier transport parameters from the lumped effective lifetime, thereby providing ac-diffusion-length-controlled depth-selective/resolved imaging.

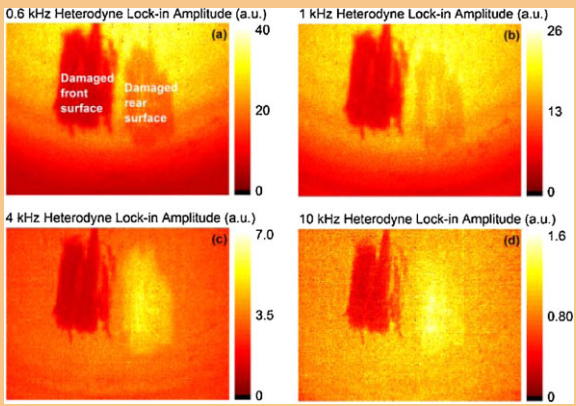

Heterodyne lock-in carrierography (LIC) amplitude images of a crystalline silicon wafer at different frequencies.

1 Introduction Camera-based luminescence imaging has been highly developed and widely used for quantitative characterization of silicon wafers and solar cells [1–5]. Dynamic photoluminescence (PL), which allows for contactless and calibration-free effective carrier lifetime imaging, can be classified as time domain (TD) and frequency domain (FD) in terms of signal detection methodologies.

The TD PL quasi-steady-state mode [6, 7], featuring slow modulation of excitation light (modulation period much longer than the effective carrier lifetime, either sinusoidal [8, 9] or square wave [10–13]), can be easily implemented with cameras, while transient PL requires wide enough detection bandwidth of the PL detector to resolve the fast temporal behavior. Kiliani et al. [14] proposed two approaches to achieve fast camera signal sampling: one is to introduce a rotating shutter wheel in front of the camera which can reach a 4-kHz maximum modulation frequency; the other is to use an InGaAs-based image intensifier unit as a fast optical shutter with which 2 kHz was attained [15]. Although the frequency upper limit in these two methods is highly improved compared with the quasi-steady-state mode, it does not encompass sufficient frequency range to resolve the values of the carrier transport parameters (bulk

lifetime, diffusivity, front and back surface recombination velocities) from the lumped effective lifetime. Pulsed-excitation transient PL is capable of separating bulk lifetime from surface recombination [16, 17], however, even today's state-of-the-art cameras cannot meet the fast sampling requirement or high signal-to-noise ratio (SNR) at short exposure time at high frequency.

Photocarrier radiometry (PCR) [18], a form of spectrally gated FD PL, uses lock-in detection to record the amplitude and phase of the photo-generated periodic carrier radiative recombination signal. By best fitting the experimental amplitude- and phase-frequency dependences, PCR has been demonstrated to be an effective quantitative methodology for carrier transport parameter determination [19–21] and carrier density imaging of Si wafers [20] and solar cells [22]. In contrast to TD PL, PCR features (i) superior SNR by virtue of lock-in detection [23]; and (ii) controllable frequency-dependent ac carrier diffusion length [18] with the potential for depth-selective/resolved imaging. Lock-in carrierography (LIC) [22], the camera-based imaging extension of the single-element detector PCR, has been demonstrated to be capable of achieving calibration-free effective carrier lifetime imaging of Si wafers [24] and contactless measurement of electrical parameters of Si solar cells [25, 26]. However, similar to TD PL, the frequency range of LIC is highly limited due to the low frame rate of state-of-the-art cameras and poor SNR at short exposure times associated with high frame rates. This limitation hinders LIC from high frequency imaging which is the key to realizing depth-selective/resolved imaging and carrier transport parameter determination.

To overcome the abovementioned limitations, a heterodyne scheme has been proposed [27, 28]. The idea is to construct a slow enough beat frequency component through frequency mixing. By virtue of the n–p product (electron–hole radiative recombination) nature [29] of the PL signal, Si-based materials and devices are natural frequency mixers for the realization of high-frequency heterodyne LIC imaging.

2 Theory

2.1 Solution of the FD diffusion equation The excess carrier density generated by square-wave modulated spread-beam optical excitation of wavelength λ is determined by the one-dimensional partial differential diffusion equation.

$$D\frac{\partial^2\Delta n(t,z)}{\partial z^2}-\frac{\Delta n(t,z)}{\tau_b}-\frac{\partial\Delta n(t,z)}{\partial t}=-G_0\beta e^{-\beta z}g(t), \tag{1}$$

where D is the ambipolar diffusivity, $\Delta n(t,z)$ is the photogenerated excess carrier density, τ_b is the bulk lifetime, $G_0=I_0(1-R)\eta/h\nu$ is the generation rate (I_0 the excitation intensity, R the reflectivity of the wafer front surface, η the optical-to-electronic quantum efficiency, $h\nu$ the photon energy), β is the optical absorption coefficient at λ, and $g(t)$ is the modulation function which has the form

$$g(t)=\frac{1}{2}+\frac{2}{\pi}\sum_{k=1}^{\infty}\frac{\sin[(2k-1)\omega t]}{(2k-1)}=\begin{cases}0, & -\frac{T}{2}\le t<0\\ 1, & 0\le t<\frac{T}{2}\end{cases}, \tag{2}$$

where T is the modulation period and $\omega=2\pi f$ is the angular frequency. The rhs expression is the Fourier expansion of a square wave. Since Eq. (1) is linear, the dc and the fundamental ac components can be separated

$$\begin{aligned}&D\frac{d^2\Delta n_0(z)}{dz^2}-\frac{\Delta n_0(z)}{\tau_b}=-\frac{1}{2}G_0\beta e^{-\beta z},\\ &D\frac{d^2\Delta n(\omega,z)}{dz^2}-(\tau_b^{-1}+i\omega)\Delta n(\omega,z)=-\frac{2}{\pi}G_0\beta e^{-\beta z}.\end{aligned} \tag{3}$$

Here the ac equation is written in complex form for simplicity. The general solution of Eq. (3) can be written as

$$\begin{aligned}&\Delta n_0(z)=C_{10}e^{-\sigma_0 z}+C_{20}e^{-\sigma_0(l-z)}-\frac{G_0\beta}{2D(\beta^2-\sigma_0^2)}e^{-\beta z},\\ &\Delta n(\omega,z)=C_1e^{-\sigma z}+C_2e^{-\sigma(l-z)}-\frac{2G_0\beta}{\pi D(\beta^2-\sigma^2)}e^{-\beta z},\end{aligned} \tag{4}$$

where $\sigma_0=(D\tau_b)^{-1/2}$, $\sigma=[(1+i\omega\tau_b)/D\tau_b]^{1/2}$, l is the wafer thickness, and C_{10}, C_{20}, C_1, C_2 are constants determined by the boundary conditions

$$\begin{aligned}&D\left.\frac{d\Delta n(\omega,z)}{dz}\right|_{z=0}=s_1\Delta n(\omega,z=0),\\ &D\left.\frac{d\Delta n(\omega,z)}{dz}\right|_{z=l}=-s_2\Delta n(\omega,z=l),\end{aligned} \tag{5}$$

where s_1 and s_2 are the front and back surface recombination velocities (SRV), respectively. The analytical expressions of the four constants in the general solution are given in the Appendix.

2.2 Homodyne PCR signal Considering the fact that the heterodyne mode is introduced in this work, here the conventional single fundamental frequency excitation PCR is called homodyne. Based on the FD carrier density solution shown above, the TD homodyne PCR signal can be expressed as a depth integral of the electron–hole density product

$$S_{ho}(t)\propto\int_0^l dz\int_{\lambda_1}^{\lambda_2}\Delta n(\Delta n+N_A)F(\lambda)S_{em}(\lambda)e^{-\beta(\lambda)z}d\lambda, \tag{6}$$

where N_A is the equilibrium majority carrier density generated by doping, $\Delta n = \Delta n_0(z) + A(\omega,z)\cos[\omega t + \phi(\omega,z)]$, $A(\omega,z)$ and $\phi(\omega,z)$ are the amplitude and phase of the photogenerated carrier density wave (CDW) $\Delta n(\omega,z)$, respectively, $F(\lambda)$ is a function of the spectral bandwidth (λ_1,λ_2) of the IR detector and filter, $S_{em}(\lambda)$ is the emitted PL spectrum, and $\beta(\lambda)$ is the near-infrared reabsorption coefficient of the radiative-recombination-emitted photons. Here the quasi-neutrality approximation is used, i.e., the photo-generated excess electron and hole densities are equal at all subsurface depths.

Lock-in detection only retains the fundamental frequency term in the integrand of Eq. (6) which has the form (in complex notation)

$$S_{ho}(\omega) \propto \int_0^l dz \int_{\lambda_1}^{\lambda_2} [2\Delta n_0(z) + N_A]\Delta n(\omega,z) \times F(\lambda) S_{em}(\lambda) e^{-\beta(\lambda)z} d\lambda. \quad (7)$$

Equation (7) indicates that beside the CDW $\Delta n(\omega,z)$, the dc excess carrier density and the dopant density also contribute to the homodyne PCR signal. Note that both the dc term $\Delta n_0(z)$ and the ac term $\Delta n(\omega,z)$ are proportional to the excitation intensity, so the dependence of the homodyne PCR amplitude on the excitation intensity can be either linear or supralinear: when $\Delta n_0(z)$ is much less than N_A at all depths in the semiconductor sample, the homodyne PCR amplitude is linear with the excitation; when $\Delta n_0(z)$ is much larger than N_A at all depths, the homodyne PCR amplitude is quadratic with the excitation intensity; when $\Delta n_0(z)$ is comparable to N_A, one can expect an approximate power dependence A proportional to I_0^{γ} with the nonlinearity exponent γ between 1 and 2.

2.3 Heterodyne PCR signal For heterodyne mixing of two angular frequencies ω_1 and ω_2 with equal optical excitation intensities, the photocarrier density $\Delta n = 2\Delta n_0(z) + A(\omega_1,z)\cos[\omega_1 t + \phi(\omega_1,z)] + A(\omega_2,z)\cos[\omega_2 t + \phi(\omega_2,z)]$. Substitute into Eq. (6) and note that lock-in detection with a reference signal at the beat frequency $\Delta\omega = \omega_2 - \omega_1$ can only retain the beat frequency component in the integrand. The TD heterodyne signal can be expressed as

$$\begin{aligned} S_{he}(t) &\propto \int_0^l dz \int_{\lambda_1}^{\lambda_2} A(\omega_1,z)A(\omega_2,z)\cos[\Delta\omega t + \Delta\varphi] \times F(\lambda) S_{em}(\lambda) e^{-\beta(\lambda)z} d\lambda, \\ &= \mathrm{Re}\left[e^{i\Delta\omega t} \int_0^l dz \int_{\lambda_1}^{\lambda_2} \Delta n^*(\omega_1,z)\Delta n(\omega_2,z) \times F(\lambda) S_{em}(\lambda) e^{-\beta(\lambda)z} d\lambda \right], \end{aligned} \quad (8)$$

where * denotes complex conjugation. By introducing β_{eff}, an effective (mean) reabsorption coefficient of the photoluminescence emission over the spectral bandwidth of the photodetector, Eq. (8) in FD can be simplified as

$$S_{he}(\Delta\omega) \propto \int_0^l dz \int_{\lambda_1}^{\lambda_2} \Delta n^*(\omega_1,z)\Delta n(\omega_2,z) e^{-\beta_{eff} z} d\lambda. \quad (9)$$

Equation (9) predicts that (i) the beat frequency term carries high-frequency CDW information; (ii) the heterodyne signal is independent of doping due to the fact that the constant dopant density cannot partake of the frequency mixing process (however, β_{eff} is doping concentration and/or contamination dependent); (iii) the amplitude of the heterodyne signal has a quadratic dependence on the excitation intensity; and (iv) the phase of the heterodyne signal $\phi(\omega_2,z)$-$\phi(\omega_1,z)$ is very small at small $\Delta\omega$, and thus difficult to be accurately measured, so the phase channel will henceforth be neglected.

3 Experimental A p-type crystalline single side-polished silicon wafer with thickness 680 μm, resistivity 25–44 Ω · cm, and with both sides oxidized in order to passivate the surfaces was used for measurements. Part of the wafer surfaces, either front or back, was mechanically damaged by rubbing with fine sandpaper.

3.1 LIC imaging system The schematic of the LIC experimental setup is given in Fig. 1. The system consists of a high-speed NIR InGaAs snapshot camera with windowing capability, two fiber-coupled 808-nm, 9-W diode lasers, a two-channel function generator, a data acquisition card, and a frame grabber. A long-pass filter, model LP-1000 nm from Spectrogon was used to block the excitation laser beams from interfering with the NIR camera. An optical block with a microlens array diffuser was used for each laser beam to homogenize the illumination intensity. The illuminated area of the wafer surface was approximately $8 \times 8\,cm^2$. Both lasers were square-wave modulated by the data acquisition card for homodyne LIC. Synchronous undersampling with external triggering of the camera was implemented for lock-in in-phase (IP) and quadrature (Q) images. Sixteen frames per correlation period were scanned and the number of skipped cycles was determined as a function of the modulation frequency.

For heterodyne lock-in imaging, the two lasers were square-wave modulated with frequencies f_1 and $f_2 = f_1 + 10$ Hz, respectively, using the two-channel function generator. Laser current modulation was activated at the first sampling instant and was stopped after each correlation period. Amplitude images were obtained from IP and Q images at the beat frequency $\Delta f = 10$ Hz.

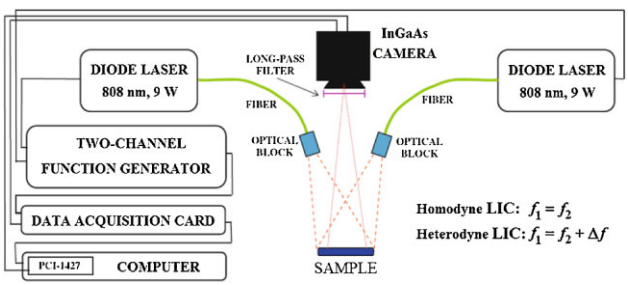

Figure 1 InGaAs camera-based LIC imaging system.

For measuring the homodyne and heterodyne amplitude dependences on excitation intensity, the laser intensity was changed by changing the iris between the collimator and the diffuser. The intensity ranged from approximately 0.12 to 0.25 W cm^{-2}.

3.2 Single-element detector system The conventional PCR system equipped with a single-element InGaAs detector and lock-in amplifier was also used for verification of the LIC results as well as for more detailed quantitative investigations and understanding of the physical mechanism(s) of heterodyne signals. In combined PCR and free carrier absorption (FCA) intensity scan measurements, an 830-nm, 30-mW focused laser was used for excitation. A density-variable rotational neutral filter was used to continuously change the excitation intensity, ranging from approximately 0.1 to 1.1 W cm^{-2}. One percent of the total laser energy was split off for intensity monitoring. The probe beam wavelength used in the FCA measurement was 1550 nm and was operated in the dc mode. A long-pass filter was placed in front of the detector to block the excitation beam. Two lock-in amplifiers measured the amplitudes of the excitation intensity and PCR and FCA signals. The same spread laser beams as in the LIC imaging system were used for measuring the homodyne and heterodyne amplitude dependences on frequency, therefore, the maximum illumination intensity was about 0.25 W cm^{-2}. Two off-axis paraboloidal mirrors collected the PCR signal from a wafer region-of-interest (ROI) and focused it on the detector which was also equipped with a long-pass filter.

4 Results and discussion The foregoing theory assumes a linear dependence of the photocarrier density on the excitation intensity. Based on the fact that the FCA signal is linear in the free carrier density, FCA measurement can reveal the carrier density versus excitation intensity behavior, shown in Fig. 2a. The ROI under investigation was at the central (intact) part of the wafer and the modulation frequency was 1 kHz. It can be seen that the nonlinearity exponent γ (the slope of the amplitude vs. intensity dependence in log–log scale) is close to 1 ($\gamma = 0.96$), which confirms the premise of the theory.

Also shown in Fig. 2a is the PCR amplitude dependence on the excitation intensity. The γ coefficient was found to be 1.6 by best-fitting. As discussed in Section 2, this value corresponds to a moderate injection level, i.e., the photocarrier density is comparable to the equilibrium majority carrier density. In fact, according to the resistivity information, the doping level of this wafer was estimated to be about 3–5 $\times$ 10^{14} cm^{-3}; the depth-averaged photogenerated carrier density under the experimental condition was estimated to be on the order of 10^{15} cm^{-3} according to the effective lifetime distribution obtained by low-frequency homodyne LIC phase images [24]. These facts show that the nonlinearity of the homodyne signal originates from the carrier-to-carrier radiative recombination.

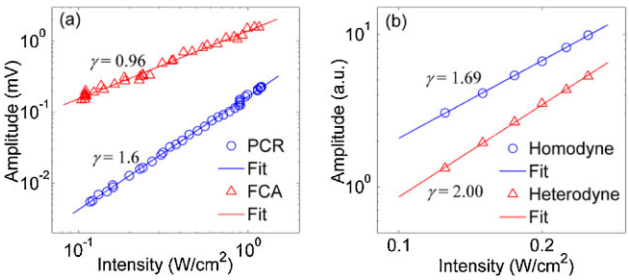

Figure 2 Dependences of carrier density, homodyne, and heterodyne PCR amplitude on excitation intensity. Carrier density was measured by the FCA method. (a) Comparison between focused-beam homodyne PCR and FCA; (b) comparison between spread-beam homodyne and heterodyne PCR. The ROI under investigation was at the central (intact) area of the wafer.

Figure 2b shows the amplitude–intensity dependences of both homodyne and heterodyne signals, measured with the camera-based LIC system. The wafer ROI was the same as that in Fig. 2a. The modulation frequency was 10 Hz for the homodyne measurement, and 1 kHz for heterodyne. It can be seen that the γ of the spread-beam homodyne signal is 1.69, slightly larger than the value measured by the focused beam single-element detector PCR system shown in Fig. 2a, while the heterodyne amplitude has an exact quadratic dependence on the excitation intensity, an excellent validation of the prediction of Eq. (9). It should be mentioned that essentially the same γ of the homodyne signal for spread and focussed beams confirms the same linear behavior of the FCA signal in the spread beam case.

Direct LIC amplitude images of the wafer at 10 and 1500 Hz are shown in Fig. 3a and b, respectively. The damaged front- and back-surface areas are characterized by small amplitudes due to significant reduction of the effective lifetime through increases in effective SRVs. LIC images can only be obtained up to 2 kHz due to the small camera signal at short exposure times at high frequencies. This upper frequency limit is not enough for separating the resolved transport parameters by multi-parameter fitting [21]. Therefore, for homodyne LIC, semiconductor samples can be characterized only by their effective lifetime [24].

The heterodyne method has the advantage of down-shifting the operating frequency of the camera within its

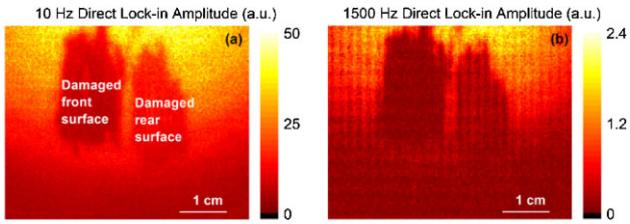

Figure 3 Homodyne LIC amplitude images at 10 (a) and 1500 Hz (b) of the wafer with mechanical front- and back-surface damaged areas.

image capturing capabilities while retaining the high frequency content (spatial resolution and contrast) of images. Heterodyne amplitude images of the Si wafer ROI of Fig. 3 obtained at 0.6, 1, 4, and 10 kHz are shown in Fig. 4a–d, respectively. The 600 Hz heterodyne image is similar to the 600 Hz homodyne image, while the 4 kHz heterodyne image differs significantly. While the area with front-surface damage is characterized by low amplitude and higher spatial resolution, the back-surface damaged area exhibits higher amplitude than the surrounding intact area. This unexpected amplitude behavior within the damaged back surface ROI can, nevertheless, be explained by the CDW penetration depth which is controlled by the ac diffusion length $L_e(\omega) = [\mathrm{Re}(\sigma)]^{-1}$. Heavier amplitude damping can occur in high-integrity regions with longer effective lifetime than that in damaged regions with shorter effective lifetime where, as a consequence, the damping rate with increasing frequency is lower.

This is further illustrated using the single-element detector heterodyne frequency scans of an intact area and a back-surface damaged area of the same wafer, shown in Fig. 5. The same contrast inversion feature as in Fig. 4 can be found. The broad frequency range allows the evaluation of the transport parameters by fitting the data to Eq. (9), using a MATLAB program which minimizes the variance of the theoretically calculated and experimentally measured data for the transport parameters inside physically reasonable ranges. The ambipolar diffusion coefficient was fixed at 18 $\mathrm{cm^2\,s^{-1}}$ as expected for crystalline silicon [30, 31]. The best-fitted parameters of the intact area data are presented in Table 1.

The bulk lifetime of the intact area of this wafer was found to be *ca.* 0.34 ms. Consistent with the fact that both surfaces of the wafer were oxidized under the same conditions, the fitted effective back SRV in the intact ROI was within the same standard deviation range as the effective front SRV, around 20 $\mathrm{cm\,s^{-1}}$. It should be mentioned that the effective re-absorption coefficient of photoluminescence emission for this wafer, β_{eff}, is higher than typical cases. This may be due to possible incipient contamination of the wafer which was quite old (several years). Tests with newer wafers produced much lower β_{eff} values, as expected.

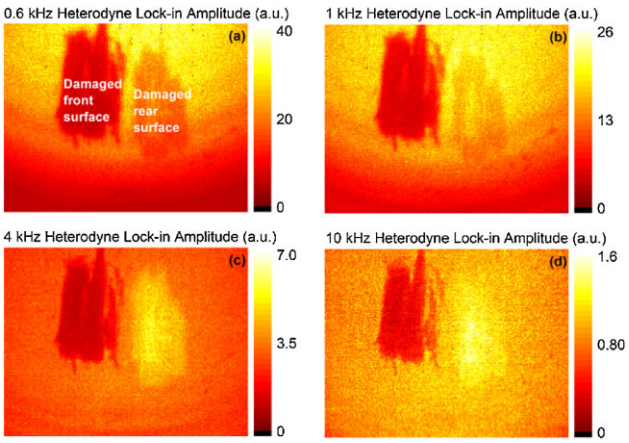

Figure 4 Heterodyne LIC amplitude images of the same wafer at 0.6 (a), 1 (b), 4 (c), and 10 kHz (d). $f_2 - f_1 = 10$ Hz.

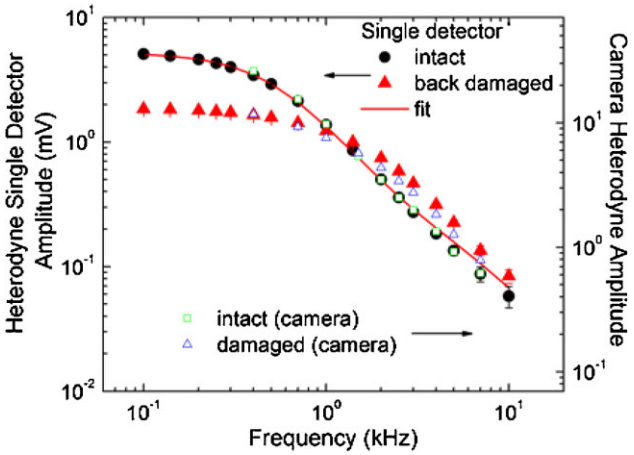

Figure 5 Heterodyne amplitude-frequency dependencies of the same wafer measured with the single-element InGaAs photodiode. Also shown are the camera pixel amplitude-frequency dependences for comparison.

For validation of the results, independent μ-PCD effective lifetime imaging (WT-2000, Semilab) of the same sample was made. It was found that the effective lifetime of the intact area of the wafer is around 0.21 ms. For comparison, the effective lifetime, estimated from the resolved transport parameters by $\tau_{\mathrm{eff}}^{-1} = \tau_{\mathrm{b}}^{-1} + [l/(s_1+s_2) + l^2/(D\pi^2)]^{-1}$, is also shown in Table 1. The estimated effective lifetime value is 0.28 ms, which is similar to the PCD lifetime.

The heterodyne frequency-dependent camera pixel signals from the same two locations with the single-element detector frequency responses show very close correspondence to the PCR response, Fig. 5. For this reason, no additional fitting procedure was performed for each pixel of the images to extract the transport parameters. The very good agreement between single-detector PCR and heterodyne LIC frequency dependencies opens the

Table 1 Transport parameters of the intact area obtained from best fitting the single-detector heterodyne frequency-scan data.

	statistical best fit	
	best fit	mean best fit
τ_{b} (ms)	0.33	0.34 ± 0.03
D ($\mathrm{cm^2\,s^{-1}}$) (fixed)	18	18
s_1 ($\mathrm{cm\,s^{-1}}$)	13	21 ± 10
s_2 ($\mathrm{cm\,s^{-1}}$)	20	17 ± 14
β_{eff} ($\mathrm{cm^{-1}}$)	33	31 ± 3
τ_{eff} (ms)	0.28	

possibility for deriving quantitative images of the major transport parameters as demonstrated with homodyne LIC [24].

5 Conclusions We demonstrated high-frequency InGaAs-camera-generated photocarrier radiative recombination images of silicon wafers by introducing quantitative heterodyne photocarrier radiometry (PCR) both experimentally and theoretically and showing agreement with the LIC pixel frequency responses. The imaging results were compared with homodyne LIC images. The near-subsurface character of high-frequency heterodyne LIC imaging can be very useful in device nondestructive evaluation. The calculated PCR effective lifetime was found to be in good agreement with independent μ-PCD measurements. The theoretically predicted quadratic dependence of the heterodyne amplitude on the excitation intensity was experimentally validated. High-frequency heterodyne LIC and the demonstrated camera pixel frequency response agreement with PCR frequency scans paves the way for quantitative optoelectronic transport property heterodyne LIC imaging, providing possibilities for depth-selective/depth-resolved imaging, and simultaneous quantitative imaging of transport properties of semiconductor substrates and devices.

Appendix

The two constants C_{10} and C_{20} in the dc solution of Eq. (4) have the form

$$C_{10} = \frac{G_0\beta}{2D(\beta^2-\sigma_0^2)}\frac{\Gamma_{20}\gamma_{10}-\gamma_{20}\Gamma_{10}e^{-(\sigma_0+\beta)l}}{\Gamma_{20}-\Gamma_{10}e^{-2\sigma_0 l}},$$

$$C_{20} = \frac{G_0\beta}{2D(\beta^2-\sigma_0^2)}\frac{\gamma_{10}e^{-\sigma_0 l}-\gamma_{20}e^{-\beta l}}{\Gamma_{20}-\Gamma_{10}e^{-2\sigma_0 l}}.$$

The two constants C_1 and C_2 in the ac solution of Eq. (4) have the form

$$C_1 = \frac{2G_0\beta}{\pi D(\beta^2-\sigma^2)}\frac{\Gamma_2\gamma_1-\gamma_2\Gamma_1e^{-(\sigma+\beta)l}}{\Gamma_2-\Gamma_1e^{-2\sigma l}},$$

$$C_2 = \frac{2G_0\beta}{\pi D(\beta^2-\sigma^2)}\frac{\gamma_1e^{-\sigma l}-\gamma_2e^{-\beta l}}{\Gamma_2-\Gamma_1e^{-2\sigma l}},$$

where

$$\Gamma_{10} = \frac{D\sigma_0 - s_1}{D\sigma_0 + s_1},$$

$$\Gamma_{20} = \frac{D\sigma_0 + s_2}{D\sigma_0 - s_2},$$

$$\gamma_{10} = \frac{D\beta + s_1}{D\sigma_0 + s_1},$$

$$\gamma_{20} = \frac{D\beta - s_2}{D\sigma_0 - s_2},$$

and

$$\Gamma_1 = \frac{D\sigma - s_1}{D\sigma + s_1},$$

$$\Gamma_2 = \frac{D\sigma + s_2}{D\sigma - s_2},$$

$$\gamma_1 = \frac{D\beta + s_1}{D\sigma + s_1},$$

$$\gamma_2 = \frac{D\beta - s_2}{D\sigma - s_2}.$$

Acknowledgements The authors are grateful to NSERC for a Discovery grant to AM, the Canada Foundation for Innovation for equipment grants, and the Canada Research Chairs. AM and QMS gratefully acknowledge the Chinese Recruitment Program of Global Experts (Thousand Talents). QMS gratefully acknowledges the project sponsored by OATF, UESTC.

References

[1] T. Fuyuki, H. Kondo, T. Yamazaki, Y. Takahashi, and Y. Uraoka, Appl. Phys. Lett. **86**, 262108 (2005).
[2] T. Trupke, R. A. Bardos, M. C. Schubert, and W. Warta, Appl. Phys. Lett. **89**, 044107 (2006).
[3] P. Würfel, T. Trupke, T. Puzzer, E. Schäffer, W. Warta, and S. W. Glunz, J. Appl. Phys. **101**, 123110 (2007).
[4] S. Herlufsen, J. Schmidt, D. Hinken, K. Bothe, and R. Brendel, Phys. Status Solidi RRL **2**, 245 (2008).
[5] J. A. Giesecke, M. Kasemann, and W. Warta, J. Appl. Phys. **106**, 014907 (2009).
[6] T. Trupke, R. A. Bardos, and M. D. Abbot, Appl. Phys. Lett. **87**, 184102 (2005).
[7] J. A. Giesecke, M. C. Schubert, D. Walter, and W. Warta, Appl. Phys. Lett. **97**, 092109 (2010).
[8] J. A. Giesecke, M. C. Schubert, B. Michl, F. Schindler, and W. Warta, Sol. Energy Mater. Sol. Cells **95**, 1011 (2011).
[9] J. A. Giesecke, B. Michl, F. Schindler, M. C. Schubert, and W. Warta, Sol. Energy Mater. Sol. Cells **95**, 1979 (2011).
[10] K. Ramspeck, S. Reissenweber, J. Schmidt, K. Bothe, and R. Brendel, Appl. Phys. Lett. **93**, 102104 (2008).
[11] K. Ramspeck, K. Bothe, J. Schmidt, and R. Brendel, J. Appl. Phys. **106**, 114506 (2009).
[12] S. Herlufsen, K. Ramspeck, D. Hinken, A. Schmidt, J. Müller, K. Bothe, J. Schmidt, and R. Brendel, Phys. Status Solidi RRL **5**, 25 (2011).
[13] S. Herlufsen, K. Bothe, J. Schmidt, R. Brendel, and S. Siegmund, Sol. Energy Mater. Sol. Cells **106**, 42 (2012).
[14] D. Kiliani, G. Micard, B. Steuer, B. Raabe, A. Herguth, and G. Hahn, J. Appl. Phys. **110**, 054508 (2011).
[15] D. Kiliani, A. Herguth, G. Micard, J. Ebser, and G. Hahn, Sol. Energy Mater. Sol. Cells **106**, 55 (2012).
[16] K. L. Luke and L. J. Cheng, J. Appl. Phys. **61**, 2282 (1987).
[17] K. Wang and H. Kampwerth, J. Appl. Phys. **115**, 173103 (2014).
[18] A. Mandelis, J. Batista, and D. Shaughnessy, Phys. Rev. B **67**, 205208 (2003).
[19] J. Batista, A. Mandelis, and D. Shaughnessy, Appl. Phys. Lett. **82**, 4077 (2003).
[20] J. Batista, A. Mandelis, D. Shaughnessy, and B. C. Li, Appl. Phys. Lett. **85**, 1713 (2004).

[21] B. C. Li, D. Shaughnessy, and A. Mandelis, J. Appl. Phys. **97**, 023701 (2005).
[22] A. Melnikov, A. Mandelis, J. Tolev, P. Chen, and S. Huq, J. Appl. Phys. **107**, 114513 (2010).
[23] A. Mandelis, Rev. Sci. Instrum. **65**, 3309 (1994).
[24] Q. M. Sun, A. Melnikov, and A. Mandelis, Appl. Phys. Lett. **101**, 242107 (2012).
[25] J. Y. Liu, A. Melnikov, and A. Mandelis, J. Appl. Phys. **114**, 104509 (2013).
[26] J. Y. Liu, A. Melnikov, and A. Mandelis, Phys. Status Solidi A **210**, 2135 (2013).
[27] A. Melnikov, P. Chen, Y. Zhang, and A. Mandelis, Int. J. Thermophys. **33**, 2095 (2012).
[28] Q. M. Sun, A. Melnikov, and A. Mandelis, Int. J. Thermophys. **36**, 1274 (2015).
[29] W. van Roosbroeck and W. Shockley, Phys. Rev. B **94**, 1558 (1954).
[30] A. Mandelis, Diffusion-Wave Fields: Mathematical Methods and Green Functions (Springer, New York, 2001), p. 586.
[31] A. B. Sproul, M. A. Green, and A. W. Stephens, J. Appl. Phys. **72**, 4161 (1992).